

# International Conference on Space Optics—ICSO 2022

Dubrovnik, Croatia

3–7 October 2022

*Edited by Kyriaki Minoglou, Nikos Karafolas, and Bruno Cugny,*



## ***MERLIN (MEthane Remote sensing LIdar missioN) – Heading towards PFM and Observation of Interesting Effects***



## MERLIN (MEthane Remote sensing LIdar missioN) – Heading towards PFM and Observation of Interesting Effects

N. Strasser<sup>a</sup>, C. Wührer<sup>a</sup>, C. Kühl<sup>a</sup>, M. Haiml<sup>a</sup>, D. Viehmann<sup>a</sup>, M. Kritzler<sup>a</sup>

<sup>a</sup>Airbus Defence and Space GmbH, Willy-Messerschmitt-Str. 1, 82024 Taufkirchen

### ABSTRACT

The Methane Remote Sensing LIDAR Mission (MERLIN) is a joint French-German cooperation on the development, launch and operation of a climate monitoring satellite, executed by the French Space Agency CNES and the German Space Agency DLR. It is focused on global measurements of the spatial and temporal gradients of atmospheric Methane (CH<sub>4</sub>) with a precision and accuracy sufficient to determine Methane fluxes significantly better than with the current observation network.

Merlin is a LIDAR Instrument using the Integrated Path Differential Absorption (IPDA) principle. This instrument principle relies on the different absorption of the laser signal by atmospheric Methane at two laser wavelengths – online and offline – both around 1645 nm, reflected by the Earth surface. The attenuation is strong at the online wavelength; the offline “reference” wavelength is selected to be only marginally affected by Methane absorption. Being an active instrument with its own light source, the MERLIN LIDAR Instrument does not rely on sun illumination of the observed areas and therefore operates continuously over the orbit.

Airbus DS GmbH was selected by DLR as the industrial Prime Contractor for the Mission Phase C/D to build the MERLIN Payload, which is the first realization of an IPDA LIDAR for space in Europe.

This presentation will concentrate on the Architecture and the Design of the MERLIN Payload, which passed the CDR in 2020 and is now progressing in Phase D. Further details of the instrument development status will be shown by an overview of the current hardware and design status of the major subsystems.

A spotlight of this paper will be a finding when performing a low-bandwidth spectral characterization of an Avalanche Photo Diode (APD), which revealed features which were not expected: Next to the known global spatial and spectral variations, the scans have shown an unexpected narrowband spectral dependence, as well as a spatial dependence, which was a factor of two worse than originally expected. Further tests also showed a thermal dependence of the QE related to the APD operating temperature, which strongly exceeded the expected variations.

These unexpected effects would have led to a highly increased Radiometric Systematic Error (RSE) in the Differential Absorption Optical Depth (DAOD).

The root-cause was identified as an Etalon effect caused by the APD substrate, which in addition varied over the APD due to slight changes in the layer thickness. The effect is strongly field angle dependent, which made a review of the scan setup necessary. Therefore, the setup was adapted via a stepwise increase of the field angle, which reduced the Etalon effect.

Consequentially, the Etalon effect as root cause for these observations has been confirmed by experiments, as well as theoretical analysis, which was shown to be in line with the measurement results.

**Keywords:** MERLIN instrument, LIDAR, DIAL, IPDA

## 1. INTRODUCTION

The joint French-German cooperation Methane Remote Sensing LIDAR Mission (MERLIN) employs an IPDA LIDAR to measure the spatial and temporal gradients of atmospheric CH<sub>4</sub> columns [1], [2] on a global scale. The satellite is being developed and operated by both countries in a joint partnership between the French Space Agency CNES and the German Space Agency DLR. A general overview on the MERLIN mission and a detailed description of the overall instrument architecture is given in [3] and [4] respectively.

The MERLIN LIDAR operates at nadir with a wavelength of approximately 1645nm, where methane has a line sextet offering suitable absorption cross sections and lineshape for implementation of a differential absorption scheme (DIAL). This is implemented by repetitive emission of dual laser pulses at slightly offset laser wavelengths, such that the on-line pulse experiences absorption from the methane feature (referred as  $\lambda_{on}$  at 1645.552 nm) and the other pulse provides a reference for the absorption of the atmospheric column outside the absorption feature (referred as  $\lambda_{off}$  at 1645.846 nm). The absolute methane content can then be inferred from the difference between the "online" and "offline" back scatter signals between instrument and scattering surface. Being an active instrument with its own light source onboard, the MERLIN Lidar instrument does not have to rely on sun illumination and can therefore continuously operate over the orbit at day and night and even through thin cirrus cloud layers [3].

The paper presented here concentrates on the design and hardware status of the MERLIN payload, as well as the latest investigations on the APD Etalon effect. The design and hardware status part of this paper is an update of the paper, which was presented at the ICSO conference in 2018, see reference document [11].

## 2. PAYLOAD DESIGN AND HARDWARE OVERVIEW

The MERLIN payload is a LIDAR instrument using the Integrated Path Differential Absorption (IPDA) principle. It relies on the different absorption at two laser wavelengths – online and offline – both around 1.645  $\mu$ m, reflected by the Earth's surface or by cloud tops. The attenuation due to atmospheric Methane absorption is strong at the online wavelength; the offline "reference" wavelength is selected to be only marginally affected by Methane absorption. The main instrument parameters are summarized in the following Table 1.

Table 1 Main characteristics of the MERLIN IPDA LIDAR instrument.

Parameter	Unit	Value
Online Wavelength	nm	1645.552
Offline Wavelength	nm	1645.846
Pulse Energy	mJ	9
Pulse Length	ns	20-30
Repetition Rate	Hz	2*20 (double pulses at 20 Hz)

The accommodation of the preliminary design of the MERLIN payload on the MYRIADE Evolutions platform is illustrated in the following Figure 1. Similar to other LIDAR instruments under development (e.g. for EarthCARE), the MERLIN instrument uses two separate telescopes for the transmission (Tx) and reception (Rx) of the laser pulses. Both telescopes are mounted on the same optical bench, which accommodates also the laser transmitter, the detection unit as well as two star trackers for verification and control of the pointing. The main structural element of the payload is the optical bench, made of CFRP and designed for maximum stiffness and lowest CTE. Primary and secondary mirrors of both Tx and Rx telescopes are made of Zerodur. The aim of the optical bench is to ensure a proper operational alignment of the two telescopes with the star tracker, and to decouple thermally and thermo-elastically the payload from platform for greater stability.

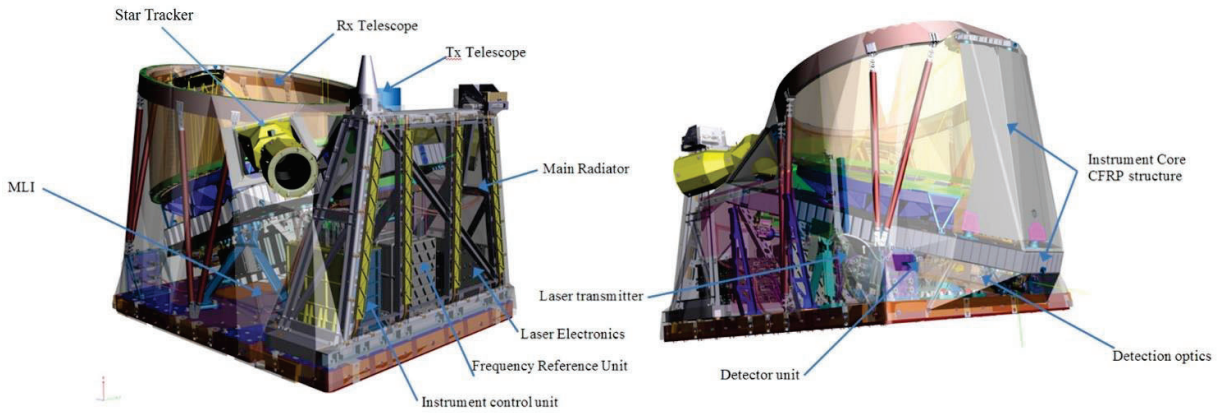


Figure 1 MERLIN Payload accommodation.

### 3. PRESENTATION OF THE INSTRUMENT SUBSYSTEM DESIGN AND HARDWARE STATUS

MERLIN payload passed the CDR in 2020 and is now progressing in Phase D. After the payload structural and thermal model (STM) was successfully assembled, integrated and tested in 2019, the project is heading towards PFM. Further details of the instrument development status are shown by an overview of the current hardware and design status of the major subsystems in this chapter. Table 2 shortly summarizes the development status of the main subsystems.

Table 2 Development status of major subsystems.

Subsystem	Supplier	Model	Status	Chapter in this paper
Laser optical bench (LASO)	ILT	EQM	Integration and assembly ongoing. Delivery expected 2023.	3.1
		FM	Delivery expected 2024.	
Laser housing (LASH)	Airbus DS	EQM	Assembly and integration finalized. Testing ongoing. Delivery expected 2023.	
		FM	Assembly and integration started. Delivery expected 2023.	
Laser (LAS = LASO and LASH)	ILT	EQM	Delivery expected first half of 2024.	
		FM	Delivery expected second half of 2024.	
Laser electronics (LAE)	vH&S	EM	Available and in use for testing since 2019.	
		PFM	Delivery expected 2024.	

Frequency reference unit (FRU)	STI	EM	Available and in use for testing since 2019.	3.2
		PFM	Delivery expected 2023.	
Internal calibration chain (ICC)	STI	QM	Delivered to instrument prime 2022.	3.3
		PFM	Delivery expected 2023.	
Instrument core	Airbus DS	PFM	Delivered to instrument prime 2020.	-
Receiver Optics (Rx)	Safran Reosc	QM	All parts were delivered to instrument prime until 2021.	3.4
		FM	All parts (except of DFL) were delivered to instrument prime in 2022. Rx telescope assembly and alignment planned for beginning of 2023.	
Transmitter Optics (Tx)	Safran Reosc	QM	All parts were delivered to instrument prime until 2021.	3.4
		FM	All parts were delivered to instrument prime in 2022. Tx telescope assembly and alignment are ongoing.	
Active pointing control (APC)	Airbus DS	PFM	Pointing Electronics delivered in 2021 Pointing Mechanism expected Q3/2022	-
Instrument control unit (ICU)	Airbus DS	EM	Available and in use for testing since 2019.	3.5
		PFM	Assembly and integration finalized 2022. Tests ongoing (finalization expected 2023).	
Signal chain SIC (= SICA and SICU)	Airbus DS	EM	Available and in use for testing since 2019.	3.6
		QM	Under qualification (finalization expected 2022).	
		PFM	Expected 2023.	

### 3.1 Laser

The design and development status of the MERLIN laser is described in detail in the article „MERLIN High Energy Laser Source for Methane Sensing at 1645 nm” of S. Hahn et al. ([10]), which is published in the same issue of these proceedings. Therefore, only a very brief summary of the design and hardware status of the laser is given below.

#### Laser optical bench – subcontracted to Fraunhofer Institute for Laser Technology (ILT)

On the top and bottom side of the laser optical bench (LASO) are the optical components that form the Nd:YAG master oscillator power amplifier (MOPA) and the subsequent optical parametric oscillator (OPO). The compliance of the concept has been validated before in air-borne LIDAR applications and ESA’s technology project FULAS [5].

The design makes use of specially developed key optical components for spaceborne lasers [4]. All mirrors, lenses and crystals – especially for the demanding components like Faraday isolator, Pockels cell, piezo actor and OPO crystal control heater – are soldered to their mounts avoiding any adhesives. These designs are inherited from the technology demonstrator FULAS.

LASO CDR was successfully passed May 2019. LASO EQM assembly and integration is currently ongoing and planned to be finalized 2023. The PFM LASO is expected to be delivered 2024.

#### Laser Housing – Airbus internal build item

The laser housing (LASH) is built as a pressurized and hermetically sealed housing with an isostatic mounting I/F for accommodation e.g. into an LIDAR instrument structure. The central frame of the housing provides several hermetical feedthroughs for electrical and optical connectors, thermal-hydraulic feedthroughs for the miniature loop heat pipes (LHP) and a beam exit window. Furthermore two connectors for purging and pressurizing the housing before final sealing are implemented. The compliance of the concept has been validated before in ESA's technology project FULAS and dedicated technology qualification activities.

Assembly and integration of LASH EQM was finalized and the testing is ongoing and should be finalized in 2023. Further, assembly and integration of the LASH FM was started and should also be finalized in 2023.

#### Laser electronics - subcontracted to von Hoerner&Sulger (vH&S)

The Laser Electronics (LAE) is the only electrical Interface (I/F) towards the Solid State Laser (LAS). It provides: control for oscillator cavity length matching to the FRU generated seed light, high power current pulses towards oscillator and amplifier pumping laser diodes, high voltage pulses to the Pockels cell, FRU input based control of the OPO cavity length, as well as thermal control of the two OPO crystals and the Loop heat pipe (LHP) cooled main heat sources on the Laser optical bench .

The delivery of LAE EM is planned for 2023, followed by PFM delivery in 2024.

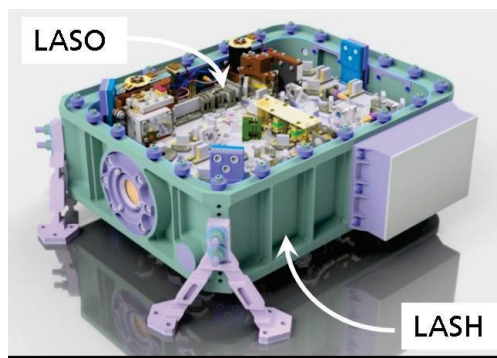


Figure 2 CAD model of laser (LAS): Laser housing (LASH) with integrated optical bench (LASO).

### 3.2 Frequency reference unit - subcontracted to SpaceTec Immenstaad (STI)

One part of the MERLIN laser system is the Frequency Reference Unit (FRU), which stabilizes the frequency of the pulsed laser relative to the absorption lines of methane at around 1645.55 nm with MHz accuracy. For the absolute reference of the online wavelength, a methane gas cell is flown within the unit. For relative frequency of the offline wavelength, a Fizeau wedge with about 4.28 GHz free spectral range (FSR) is used, being part of a wavemeter. Low noise laser diode drivers have been developed and implemented in order to keep the laser frequency within the desired accuracy range. Also, the MERLIN master oscillator is seeded by the FRU with narrowband 1064 nm laser light.

The major functional and performance requirements of the FRU are: seeding of the 1064 nm master oscillator, absolute frequency referencing to the 1645.55 nm methane line and seeding of the OPO at the two wavelengths,  $\lambda_{on}$  and  $\lambda_{off}$ , spectroscopic measurement of every individual OPO laser pulse, providing a frequency knowledge better than 8 MHz for the online and 50 MHz for the offline frequency and control and stabilization of the instrument's OPO cavity length according to the performed measurements.

The FRU has an envelope of 237 x 190 x 232 mm, a mass of <6.2 kg and an operational power dissipation of <23 W. The command and control interface to the spacecraft ICU is via a SpaceWire interface. A reprogrammable FPGA is used in order to control and operate the unit after the ICU has initialized and commanded it. Different implemented modes serve for operation, calibration and diagnostics.

The FRU completed its Critical Design Review (CDR) in July 2018. Afterwards, the flight-design representative Engineering Model (EM) FRU was successfully tested and delivered to the instrument prime in 2019. The PFM FRU is planned for delivery in 2023.

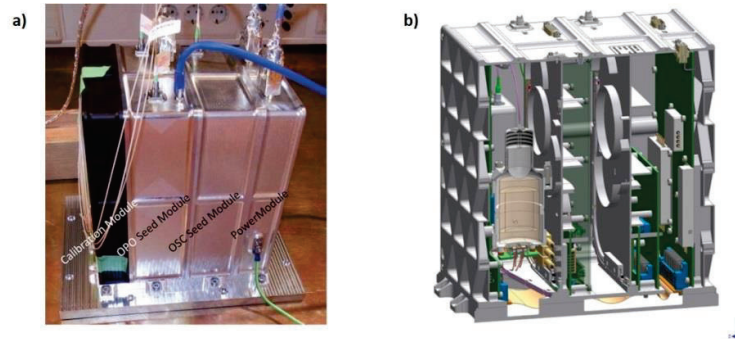


Figure 3 a) Mechanical design of the FRU overall system (EM at EMC test). b) Cut-away view of the FRU assembly.

### 3.3 Internal calibration chain - subcontracted to SpaceTec Immenstaad (STI)

The Internal Calibration Chain (ICC) is used to provide fractions of the emitted laser beam to the Signal Chain, as well as the Frequency Reference Unit, in order to determine the following information: 1) Radiometric reference signal, 2) Tx laser pulse time stamp and 3) Tx laser pulse frequency.

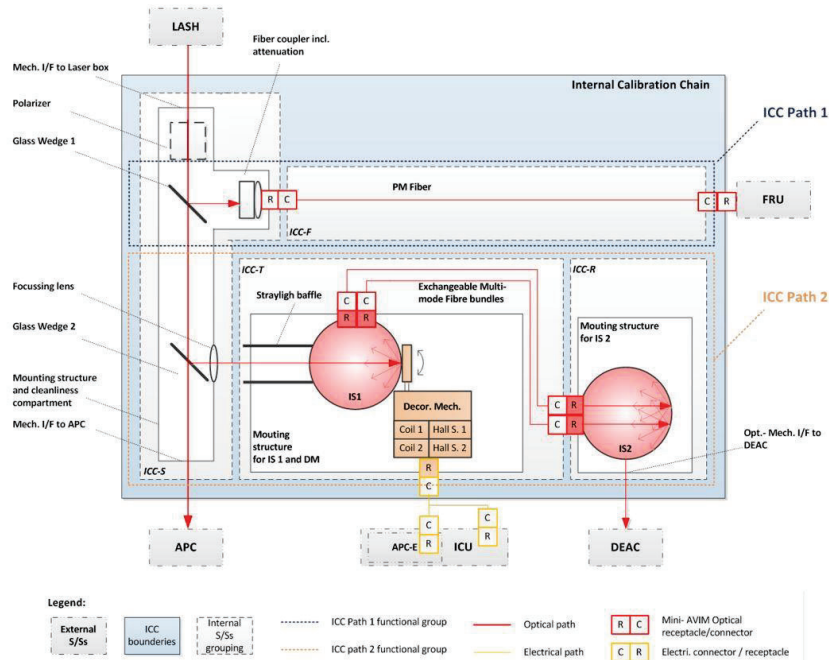


Figure 4 ICC schematic setup.

Tasks (1) and (2) is assigned to the ICC path 2. Task (3) is assigned to the ICC path 1, which are schematically shown in Figure 4.

The dominating performance aspect of the ICC is the radiometric energy references for the IPDA. Here a huge effort was spend to meet the dynamic range of the signal chain and to minimize the systematic errors in this subsystem. Important elements to be addressed in order to achieve this systematic error free concept for the two wavelengths are error sources like coating variations, etalon effects and speckle statistics.

For the speckle topic a dedicated decorrelation mechanism is used to generate independent start conditions for the phase correlation of the two pulses. This mechanism is realized by a moving diffusor at the first scattering surface of the reference path.

The ICC completed its Critical Design Review (CDR) in June 2021. Afterwards, the Qualification Model (QM) ICC was successfully qualified and delivered to the instrument prime in 2022. The PFM ICC is planned for delivery in 2023.



Figure 5 Left) ICC HW status decorrelation mechanism. Middle) Integrating sphere. Right) Transfer fiber bundle.

### 3.4 Optical subsystem - subcontracted to Safran Reosc

The Merlin optical concept is based on a bistatic concept for Tx and Rx path.

The receiver telescope RX is an afocal design with a magnification of 50x. It consists of two conical mirrors and an achromatized ocular lens (OCL). A design driver has been the need for a compact envelope allowing a maximal M1-M2 mirror distance 470mm. The Detector Focusing Lens (DFL) focuses the collimated light from the exit pupil onto the detector. Due to the scientific specifications of low detection noise (small detector) and large ground spot a very low  $f\#$  of  $<0.65$  for the DFL was required, which was one driving factor for the Rx design.

The transmitter telescope consists of the primary TXOTP (M1) and secondary TXOTS (M2) transmitter mirrors, an optical cover window (TXOW), and an active pointing control mirror (APC). The TXOW is required for contamination protection and the APC is necessary for active in orbit co-alignment between the RX and TX beams.

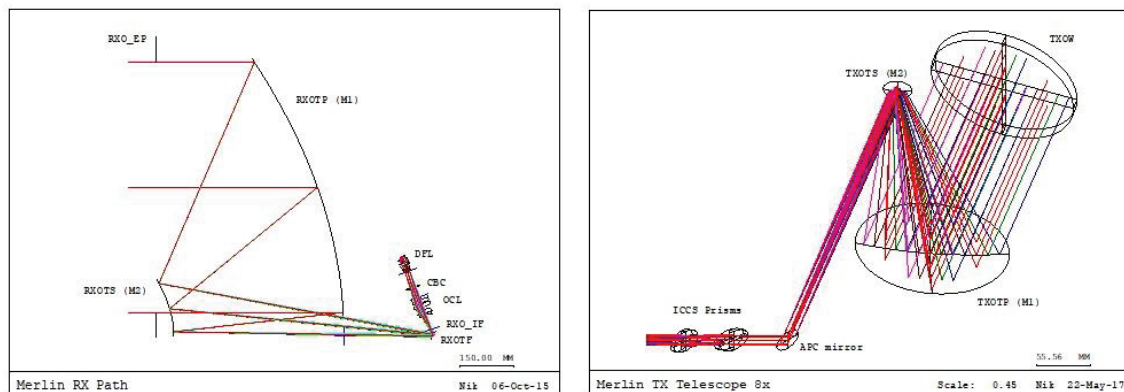


Figure 6 Left) Overview of the Rx path. Right) Overview of the Tx path.

Safran Reosc has been selected as our subcontractor for all of the RX and TX telescope optics, including the lens packages OCL, DFL and DEAC. One supplier for all main components allowed us to find the best balanced solution for the RX and TX optics that ensures a good feasibility and an efficient manufacturing for all design aspects.

Safran Reosc's critical design review (CDR) has been successfully passed in 2017. Qualification models (QM) of all optical elements of the Tx and Rx path were successfully manufactured and tested until 2021. Further, all flight model (FM) elements (except of DFL) were manufactured and delivered to the instrument prime. The FM Tx telescope assembly and alignment is currently ongoing on the FM Rx telescope assembly and integration will follow beginning of 2023.

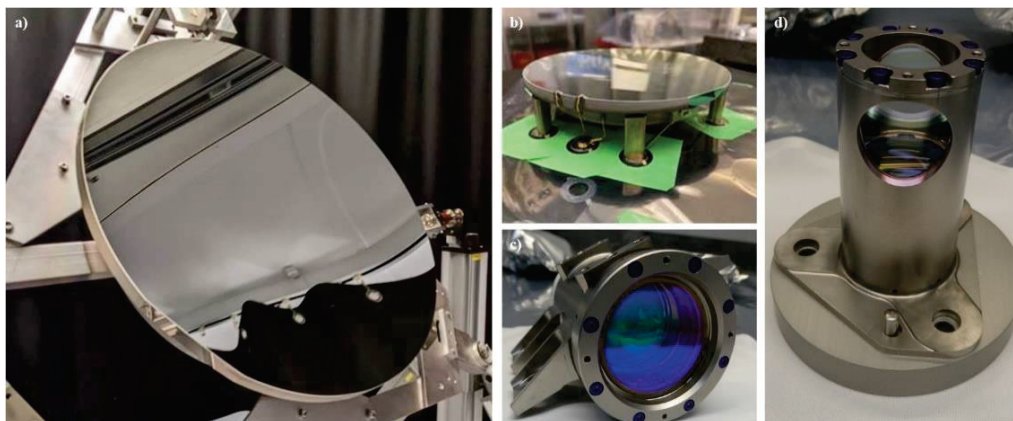


Figure 7 a) Rx M1 FM mirror, b) Tx M1 FM mirror, c) OCL FM, d) DEAC CBC FM.

### 3.5 Instrument control unit - Airbus internal build item

The Instrument Control Unit (ICU) with the included DCM module of the Signal Chain (SIC), is the sole command interface between the platform and the instrument. It provides the command interface and the science data interface. The command interface will be used to receive commands and to send telemetry. The science data interface will be used to provide the measurement data and all ancillary data, which is required for the on-ground processing of the measurement data (e.g. timestamps, signal energy data, detector temperature, etc.).

The ICU makes use of recurring modules, with the exception of the SIC including the DCM, which is instrument specific.

To date, the ICU EM was successfully assembled, integrated and tested. Also the integration and assembly of the ICU PFM was finalized and testing is currently ongoing (plan to be finalized beginning 2023).



Figure 8 Merlin instrument control unit – PFM.

### 3.6 Signal chain - Airbus internal build item (InGaAs-APD: Laser Components Detector Group, Inc.)

The signal chain (SIC) is in charge of acquiring the laser pulses during various stages. It consists of a focal plane incorporating an InGaAs-APD detector mounted in its housing (signal chain assembly = SICA), the analogue signal processing proximity electronics (signal chain unit = SICU) and the signal processing chain including the ADC, which is physically contained in the ICU (DCM module), as introduced above. There are two types of data products which need to be extracted from the measurement: the total absolute signal energy and the turnaround time (and thus the path length). Effectively, the ratio between transmitted (Tx) and received (Rx) signals, and online/offline are used for determination of the CH<sub>4</sub> mixing ratio. The main processing steps of the Signal Chain after are:

- Co-addition of the individual pixel values (within each sampling period [“vertical”]),
- Acquisition, time stamping, PUS and CCSDS SpW formatting of measurement data, configuration data, and ancillary data packages originating from the other sub-units
- Sorting of the data, coming from the different data sources, into the mission data stream and output of the data to the P/F Mass Memory.

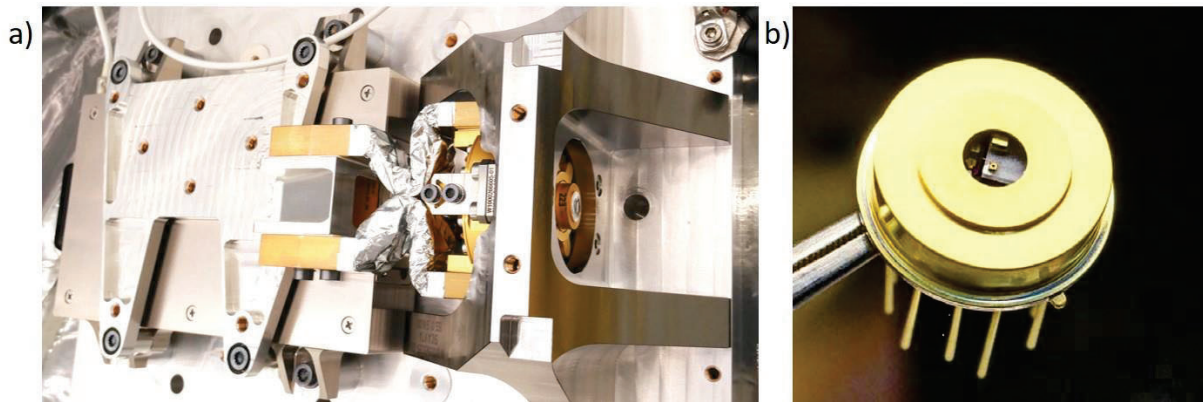


Figure 9 a) MERLIN SIC (SICA+SICU) QM. b) APD detector EM.

To date the radiometric resolution performance and the non-linearity calibration has been confirmed with the selected combination of detector, front-end electronics and A/D converter EM. Further, the qualification tests of the SIC QM are ongoing and are planned to be finalized in Q4 2022. In parallel to the SIC QM tests, the PFM APD selection process was ongoing (surface scans), which have led to unexpected investigations, which are described in detail in the next chapter.

## 4. ETALON EFFECT CAUSED BY THE APD SUBSTRATE

### 4.1 Context of Observation

In the frame of the PFM APD selection process, APD surface scans were conducted. Next to the known global spatial and spectral variations, the scans have shown an unknown narrowband spectral dependence (interference fringes), as well as a spatial dependence, which was a factor 2 worse, than originally expected (see Figure 10). Further, also a thermal dependence of the QE related to the APD operating temperature was identified. These unexpected effects would have led to a highly increased RSE DAOD contribution, which would have risked a RSE non-compliance. Therefore, it needed to be analyzed, if this is due to a partly non-representative setup or also a real risk for the operational instrument. Chapter 4.3 describes the measurement results of the unknown and unexpected effect, as well as the potential impact on the RSE contribution.

The root-cause was identified as an Etalon effect caused by the APD substrate, which in addition varied over the APD due to slight changes in the layer thickness.

The Etalon effect as root cause for these observations has been confirmed also via theoretical analysis, which are in line with the measurement results. The theoretical analysis is described in chapter 4.4.

This effect is strongly Angle of Incidence (AOI) dependent, which made a review of the scan setup necessary. The AOI was much smaller ( $\pm 8^\circ$ ) than the operational MERLIN AOI ( $\pm 48^\circ$ ). Therefore, the setup was adapted via a stepwise increase of the AOI, which reduced and therefore confirmed the theory of the Etalon effect.

Based on the detailed understanding of the Etalon effect and its root-cause investigations on the impact on the overall instrument performance have been conducted based on the most representative AOI, which can be reached within the setup boundaries. It has been shown, that already for this AOI the instrument performance gets even better, than expected for the CDR.

In summary, all these investigations were important to guarantee a representative setup for the PFM SIC characterization and calibration measurements, which is not affected by this Etalon effect.

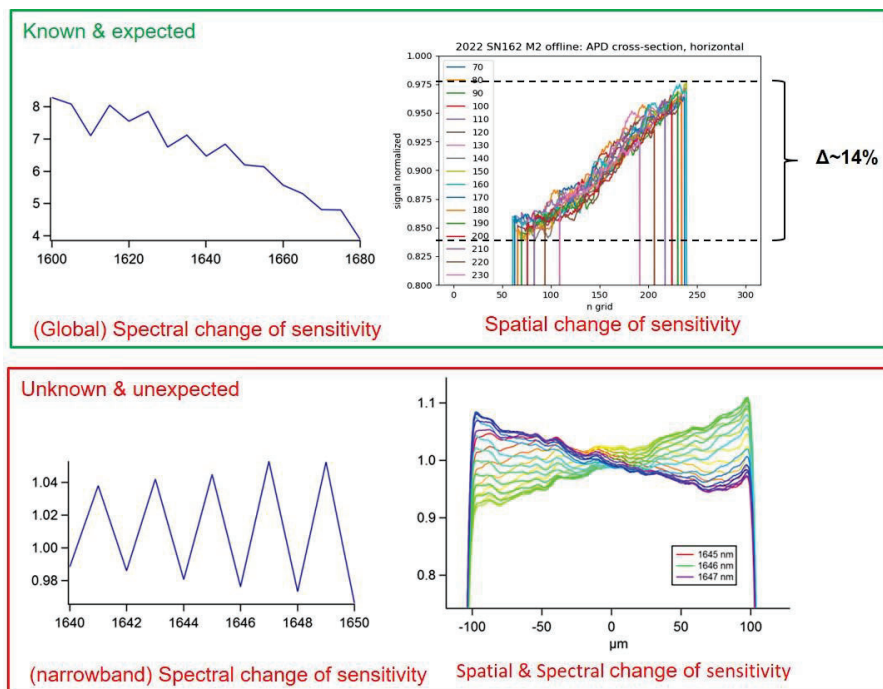


Figure 10 Summary of known and unknown APD characteristics.

### 4.2 Setup and device under test description

The APD surface scan setup during these tests is schematically shown in Figure 11. It allowed a surface scan in 1 μm steps (300x300 steps) and consisted of an OGSE as illumination system (i. e. laser, attenuator, photodiodes and alignment tool), MGSE for controlling the position of the alignment tool during the scans (i. e. piezo rack) and an EGSE for command, control and readout of the MERLIN detection chain (i.e. ICU EGSE, PC, Peltier BoB). The electronics under test were ICU, SICU and SICA EM.

Theoretical and data based investigations on the observed unknown and unexpected effect (see Figure 10) have led to the assumption, that this Etalon effect is caused by an interference within the APD substrate, which is AOI dependent. Therefore, the idea was to increase the AOI of the setup stepwise from originally +/-8° close to the operational AOI of +/-48° via changing the focusing lens within the scan setup. Due to the limited space within the setup, the largest (and therefore most representative) AOI, which can be reached is +/-30.3°. Table 3 summarizes the focal length of the different focusing lenses and their resulting Airy disc diameter on the APD as well as the corresponding AOI.

For the Airy disc diameter and AOI calculations a fibre NA of 0.14 and a collimator focal length of 18.75 mm are used, which lead to a beam diameter of 5.25 mm. The parameters in Table 3 are calculated via

$$D_{Airy} = 2.44 * \lambda * \frac{f}{D_{beam}}$$

$$AOI = \tan^{-1}\left(\frac{D_{beam} * 0.5}{f}\right)$$

Table 3 Airy disc diameter and AOI for the different focusing lenses.

Focal length [mm]	Airy disc diameter [μm]	AOI [+/-°]
18.4	14.1	8.1
7.5	5.7	19.3
4.5	3.4	30.3

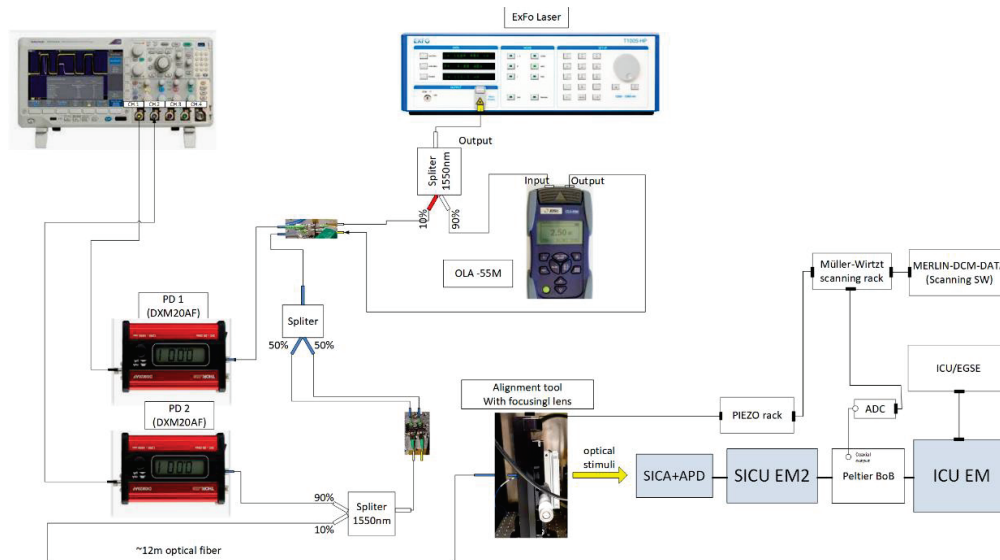


Figure 11 Block diagram of overall test setup.

### 4.3 Description of measurements

#### Spatial dependence of sensitivity

Figure 12 shows the horizontal (upper row) and vertical (lower row) cross-sections of the APD QE measured with the online wavelength (left column) and offline wavelength (right column). The data is acquired with the APD model SN162 (this model will be used for the rest of the document) for gain 2 and at room temperature. As visualized in the first row of Figure 12, the slope of the QE behaves differently for the two wavelengths. Figure 13 a) visualizes this wavelength dependent difference for 2 perpendicular cross sections. This wavelength dependent difference was unexpected until this measurement and can lead to a higher systematic error on instrument level, which was not taken into account until now. The quantitative RSE impact of the spatial and spectral dependence of the APD is simulated and the results are described later on in this chapter.

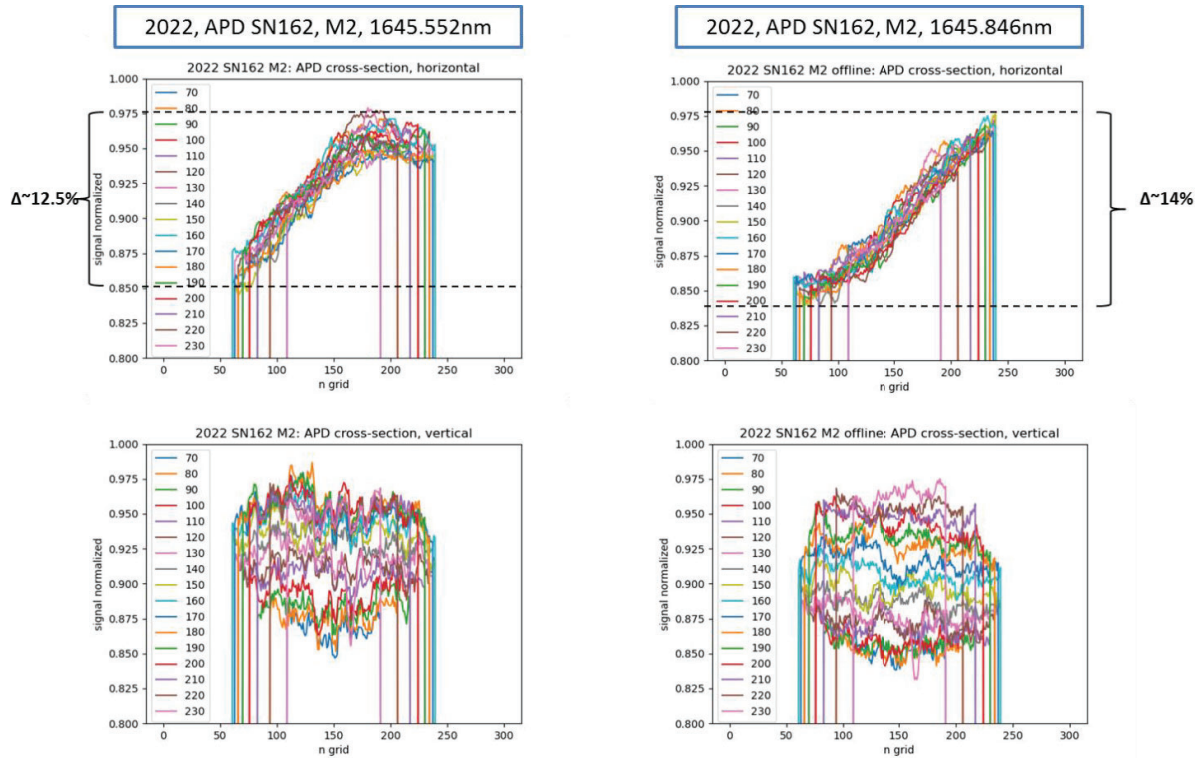


Figure 12 Comparison of the APD QE map (cross-sections) for online wavelength (left) and offline wavelength (right).

#### Spectral dependence of sensitivity

For a better understanding of the spectral dependence of the APD QE, the responsivity was measured for a larger wavelength regime. Whereas Figure 13 b) shows the known bandgap of the APD InGaAs substrate, Figure 13 c) shows an unexpected spectral fringing pattern with a spectral modulation of  $\sim 2\text{nm}$ . For a better understanding of the narrowband spectral and spatial dependence of the QE, the APD QE scan was acquired in small steps between 1645 and 1647 nm (see Figure 13 d)). The plot reveals unexpected spatial and spectral dependence of the APD QE, which will be analyzed in the following chapters (theoretically and per test).

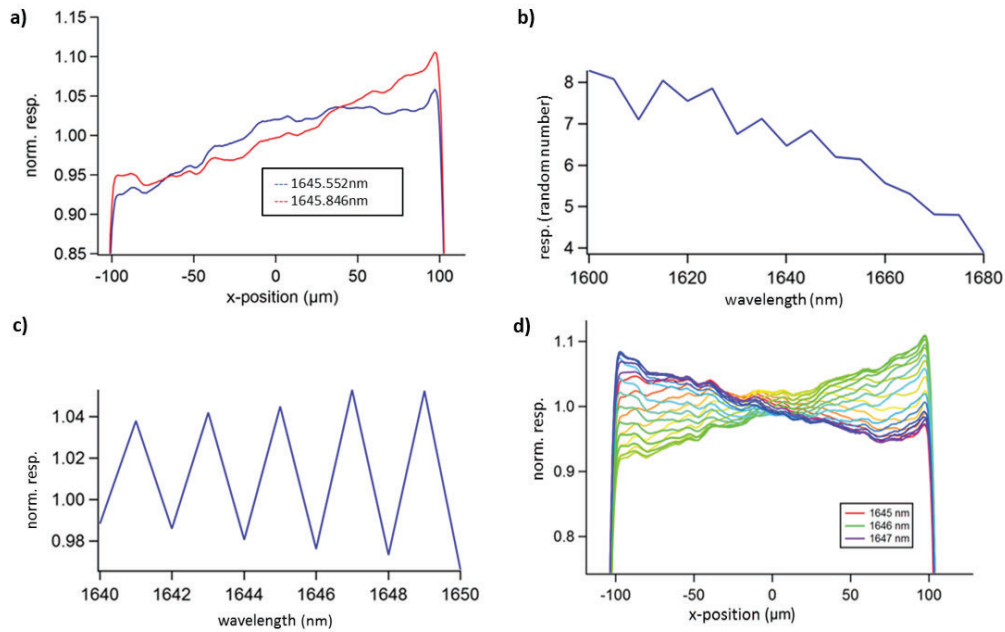


Figure 13 a) Cross section of APD QE map for online and offline wavelength. b) Visualization of the bandgap. c) Detailed zoom in plot c), interference effect. d) Spatial APD QE scan for different wavelengths.

### Temperature dependence of sensitivity

The impact of temperature on the fringing has been investigated. The rationale for the test series with 1K steps was to further verify the hypothesis, that the observed etaloning is at the origin of the InP substrate cavity. The cavity mirrors are assumed to be the backside coated gold reflector and frontside residual reflection from the APD multilayer structure, mainly the 1550nm optimized single layer AR-coating. The temperature dependent refractive index of InP is known from literature and a phase shift of the fringing pattern of about  $\pi$  would be expected. Note, that the change of effective optical length of semiconductor cavities is usually dominated by the refractive index change and only to a less impact by the thermal expansion (CTE). For  $\sim 200\mu\text{m}$  InP a temperature increase of about 20K is necessary to increase the cavity length by  $\lambda/2$  (shift of one free spectral range). Hence, we would expect a phase shift of about  $\pi$  for a cool-down from room temperature (RT, 22°C) to the APD operational temperature of 10°C. For a quantitative analysis, see the chapter 4.4 below.

Certainly, in addition to a temperature series, the objective was also to characterize the etaloning at Merlin APD operational temperature of 10°C.

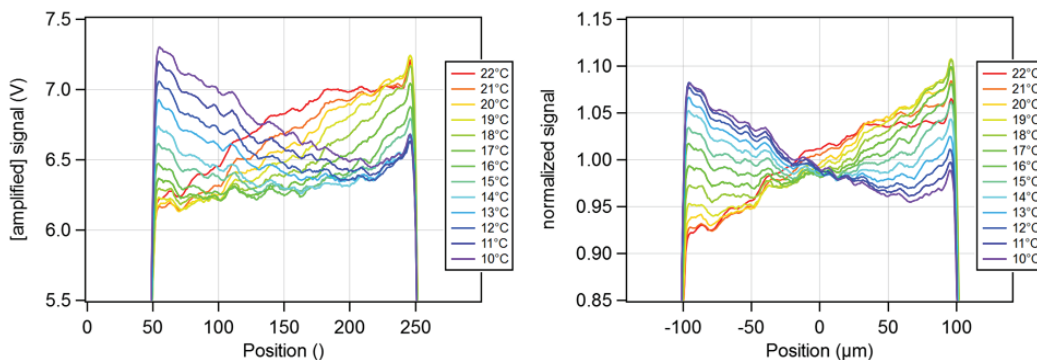


Figure 14 Spatial APD QE scan for different APD temperatures.

### Interpretation of the measured effect

Based on the spectral fringing with a spectral modulation of  $\sim 2\text{nm}$  shown in Figure 13 b), the root-cause seems to be an Etalon effect, induced by the Indium Phosphide (InP) substrate in the APD.  $2\text{nm}$  spectral modulation corresponds to a physical etalon thickness of  $d = \lambda^2 / (2 n \Delta\lambda) \sim 200\mu\text{m}$ , with  $n$  being the averaged index of refraction of the substrate.

The modulation amplitude is around 10%, which can be used to calculate Finesse (defined by the reflectivity of the interfaces).

Further, half of an interference-ring distance can be observed between the left and the right side of the APD (see Figure 13 d)). This leads to the assumption, that the difference in the Etalon substrate thickness between the left and the right side of the APD is  $\sim 130\text{ nm}$ . (An increase of the Etalon substrate thickness of  $\lambda/4$  leads to an intensity change from maximum to minimum, what can be observed between both sides of the APD. For the MERLIN wavelength of  $1646\text{ nm}$  this means  $1646\text{ nm}/4 = 411\text{ nm} \rightarrow$  divided by an InP refraction index of  $3.15 \rightarrow$  difference in substrate thickness between left and right side of the APD =  $130\text{ nm}$ .)

The interference furthermore changes with temperature. Two effects contribute: the thermal expansion of InP ( $4.6\text{e-}6 / \text{K}$ ) and the temperature dependent change of refractive index ( $2\text{e-}4 / \text{K}$ ). In the present system, the temperature dependent refractive index has a significantly higher impact, than the thermal expansion.  $\Delta n/n = 2\text{e-}4 * 12 = 0.0024$ . Consequently, the effective thickness  $d \cdot n(T)$  changes by about  $\lambda/4$ , consistent with the observed phase shift of  $\sim \pi$ .

Based on this assumptions a detailed theoretical analysis was conducted, where a slope in the InP substrate in the APD of  $\sim 130\text{ nm}$  was simulated to see, if this measured Etalon effect can be quantitatively and qualitatively explained by this theory. The details and the results of this analysis are summarized in section “Simulation of the Etalon effect” below. The analysis has confirmed this assumption and could also prove the dependence of this effect on the AOI of the illumination.

Therefore, the setup was re-checked with respect to the existing AOI. Like already described chapter 4.2 the AOI of the current setup only covered  $\pm 8^\circ$ . Therefore, the idea was to increase the AOI of the setup stepwise from originally  $\pm 8^\circ$  close to the operational AOI of  $\pm 48^\circ$  via changing the focusing lens within the scan setup. Due to the limited space within the setup, the largest (and therefore most representative) AOI, which can be reached is  $\pm 40.3^\circ$ .

The following chapters are describing the measurement results for different focusing lenses with focal lengths of  $7.5\text{ mm}$ ,  $4.5\text{ mm}$ ,  $3.1\text{ mm}$ , which corresponds to AOI of  $\pm 19.3^\circ$ ,  $\pm 30.3^\circ$ .

### Impact on instrument performance: Relative Systematic Error (RSE)

In this section the impact of the new identified Etalon effect on the overall instrument performance is analyzed. The instrument performance is mainly driven by the Relative Systematic Error (RSE), which combines the measurement error contributors due to detection chain non-linearity ( $RSE_{NL}$ ), coalignment errors, Rx coating effects, particles, APD QE inhomogeneity ( $RSE_{TxRxAlign\_APDnonuniform}$ ), receiver path ghost effects ( $RSE_{ghosts}$ ) and calibration paths transmission effects ( $RSE_{ICC}$ ).

$$RSE = \sqrt{RSE_{NL}^2 + RSE_{TxRxAlign\_APDnonuniform}^2 + RSE_{ICC}^2 + RSE_{ghosts}^2}$$

Until the new APD QE maps were measured starting in December 2021 the APD QE map from 2017 was used as input for the RSE calculations. Only one APD map was used for online and offline wavelength and the slope was only  $\sim 7\%$ . Based on this QE map, the RSE contributor  $RSE_{TxRxAlign\_APDnonuniform}$  was calculated via a Monte Carlo pointing simulation, which summarizes the error contributors due to pointing errors, clipping, particles and APD non-uniformity.

The value for  $RSE_{TxRxAlign\_APDnonuniform}$  is determined for a pulse pair offset from the APD center of  $15\text{m}$ , an offset between both pulses of  $40\mu\text{rad}$  and for a PSF without defocus. For the analysis based on the APD map from 2017, the  $RSE_{TxRxAlign\_APDnonuniform}$  is  $0.025\%$  (see black circle in Figure 15 a)), whereas for the value based on the new APD QE maps reaches  $0.114\%$  (see black circle in Figure 15 b)).  $RSE_{TxRxAlign\_APDnonuniform}$  alone nearly reaches the overall RSE spec value of  $0.13\%$ .

Nevertheless, the assumption, which was already confirmed via analysis, was, that this effect occurs due to the small AOI in the test setup and should decrease drastically for representative AOI close to  $\pm 48^\circ$ . Therefore, the following

measurements with larger AOI were conducted to increase the AOI and assess the RSE based on representative QE maps.

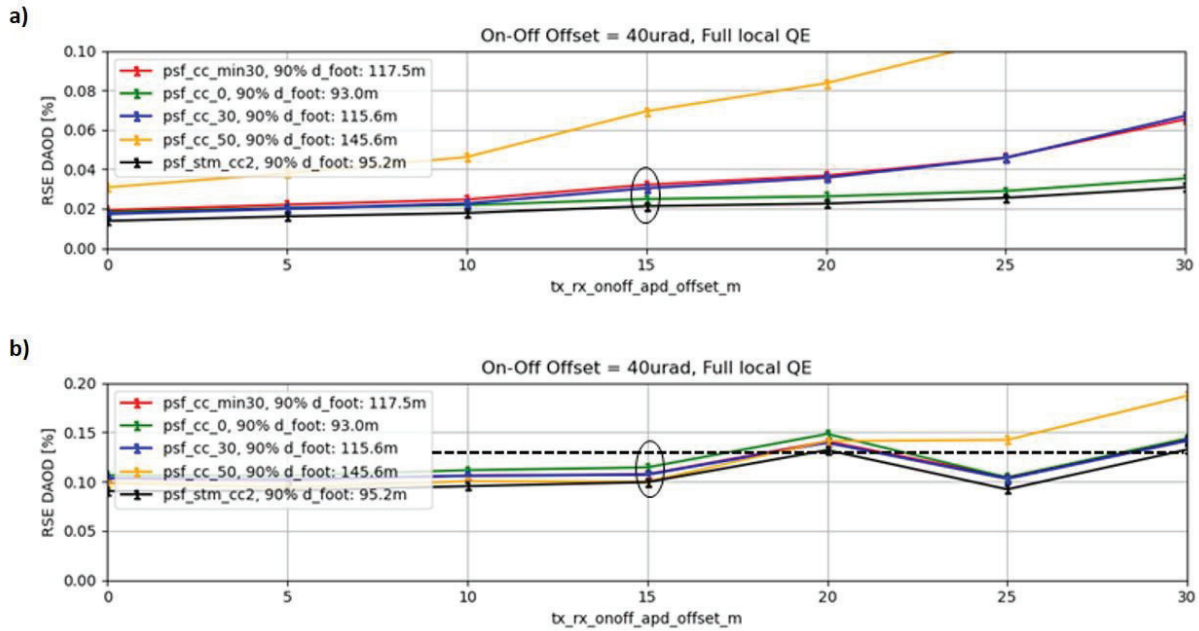


Figure 15 a)  $RSE_{TxRxAlign\_APDnonuniform}$  DAOD due to pointing/cliping and APD QE with one APD map for online and offline wavelength and 18.5mm lens. b)  $RSE_{TxRxAlign\_APDnonuniform}$  DAOD contribution due to pointing/cliping AND new separate APD QE maps for online and offline wavelength. The black dotted line indicates the overall RSE spec value.

### Dependence of Etalon effect on Angle of Incidence (AOI)

Figure 16 shows the cross-section of the APD QE map for the new installed focusing lens of 7.5mm (middle plot) and 4.5mm (right plot) in comparison to the already known APD QE maps for the original 18.4mm lens (left plot). As assumed already via analysis, the slope reduces drastically with the increase of the AOI.

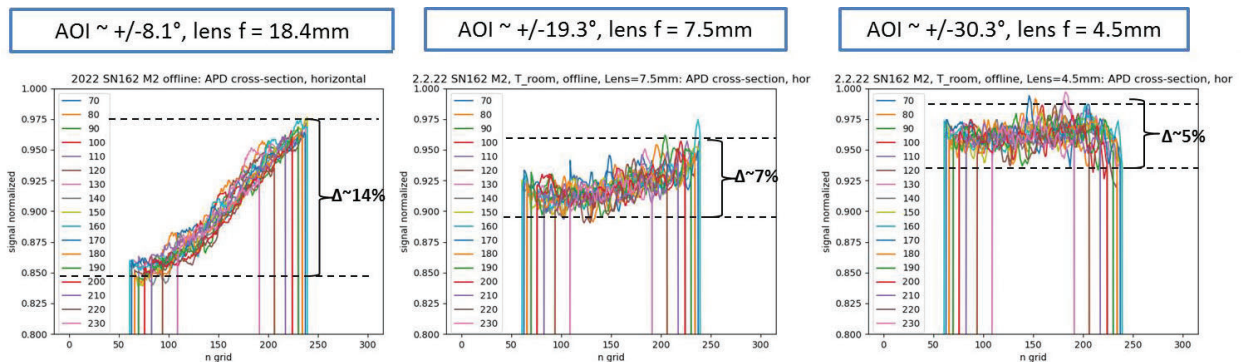


Figure 16 Comparison between the APD QE cross-section for the original 18.4mm lens (left), 7.5mm lens (middle) and the 4.5mm lens (right).

Again,  $RSE_{TxRxAlign\_APDnonuniform}$  is determined for a pulse pair offset from the APD center of 15m, an offset between both pulses of 40 $\mu$ rad and for a PSF without defocus.

For the analysis based on the APD map from 2017,  $RSE_{TxRxAlign\_APDnonuniform}$  is 0.025% (see black circle in Figure 15 a)), whereas it is decreased to 0.017% based on the new APD QE maps (see black circle in Figure 17).

Even if the AOI (+/- 30.3°) is still not completely representative to the operational AOI of +/-48°, the  $RSE_{TxRxAlign\_APDnonuniform}$  contributor due to APD non-uniformity is better than assumed for CDR and the last Performance Working Group and therefore also the overall RSE DAOD is better than expected.

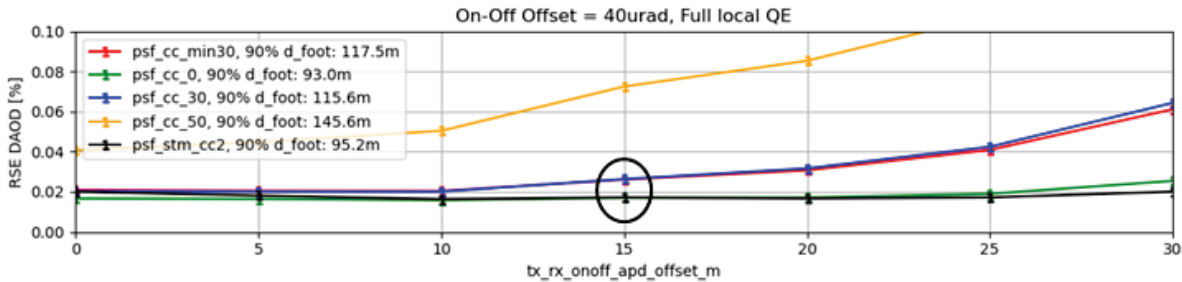


Figure 17  $RSE_{TxRxAlign\_APDnonuniform}$  due to pointing/clipping and APD QE with different APD maps for online and offline wavelength and 4.5mm lens.

#### 4.4 Simulation of the Etalon effect

The quantitative (numerical) analysis of the etalon effect was performed with a semi-analytical model consisting of two major parts, i.e., a model for the detector and a model for the Gaussian beam. The layout of the detector has been obtained by reverse engineering, at least for the optically relevant layers, which are InGaAs, where the conversion from photons to electrons takes place, Indium Phosphide (InP) with a thickness of several hundred  $\mu$ m, followed by a stack of Silicon and Gold which is – for the case of simplicity – considered as an ideal reflector with  $R = 100\%$ .

The incident radiation is described by a Gaussian beam of wavelength  $\lambda_{on}$  and  $\lambda_{off}$ , beam waist  $w_0$  (or  $\sigma_0$ ), and quantities like angle of divergence (or  $f\#$ ) that can be derived from the previous quantities. The incident radiation is focused on the first (surface) layer of the multilayer stack. Inside the various media of the detector layer stack (which are characterized by refractive indices  $n_i$  and thicknesses  $d_i$ ) the beam (cone) is refracted according to Snell's law, thus leading to a much narrower cone angle than in ambient environment. As soon as the incident radiation enters the InGaAs layer a significant fraction of the incident power is absorbed and converted into photoelectrons. The remaining power propagates up to the Si/Au layer where it is reflected (assumption:  $R = 100\%$ ). After propagating back to the InGaAs layer the remaining power will finally be absorbed a second time. The effect of etaloning is numerically modelled by an interference of the incident electric field with the fraction that has been reflected from the Si/Au layer while properly considering the phase difference that occurs as well as the attenuation of the reflected electric field due to the partial absorption during the first pass through the InGaAs layer and (divergence angle dependent) defocusing. The complex electric field distribution of a Gaussian beam may be expressed in cylinder coordinates as:

$$E(\rho, z) = E_0 \left( \frac{\sigma_0}{\sigma(z)} \right) e^{-\left( \frac{\rho}{\sigma(z)} \right)^2} e^{-ik \frac{\rho^2}{2R(z)} - i(kz - \zeta(z))}$$

$$k = \frac{2\pi n}{\lambda}$$

$$z_R = \frac{k\sigma_0^2}{2}$$

$$\sigma(z) = \sigma_0 \sqrt{1 + \left( \frac{z}{z_R} \right)^2} = \sigma_0 \sqrt{1 + \left( \frac{2z}{k\sigma_0^2} \right)^2}$$

$$R(z) = z \left( 1 + \left( \frac{z_R}{z} \right)^2 \right) = z \left( 1 + \left( \frac{k\sigma_0^2}{2z} \right)^2 \right)$$

$$\zeta(z) = \arctan \left( \frac{z}{z_R} \right)$$

where  $\lambda$  is the wavelength, and  $n$  the refractive index of the etalon. The standard deviation of the Gaussian function  $\sigma_0$ , is linked to the (more commonly used) beam waist  $w_0$  by

$$\sigma_0 = \frac{w_0}{\sqrt{-2 \ln(1 - V/100\%)}}$$

where  $V$  specifies the percentage of the encircled energy up to mentioned diameter  $w_0$  (and thus defines  $w_0$  implicitly). For  $V$  usually a value of 90% is taken.

By evaluating the general expression for the Gaussian electric field at  $z = 0$  we get the expression for the incident field:

$$E_{Incid}(\rho, z) = E(\rho, z = 0) = E_0 e^{-\left(\frac{\rho}{\sigma_0}\right)^2}$$

The corresponding expression for the reflected field is given by

$$E_{Etalon}(\rho, z) = \tau E(\rho, z = 2d_{InP})$$

Where  $d_{InP}$  is the thickness of the InP layer and  $\tau$  the transmission of the electric field after having passed the InGaAs layer where the field is attenuated. The total electric field is given by the coherent sum

$$E_{tot}(\rho, z = 0) = E_{Incid}(\rho, z = 0) + E_{Etalon}(\rho, z = 2d_{InP})$$

The (physically relevant) irradiance is proportional to the absolute square of the electric field

$$I_{tot}(\rho, z = 0) = |E_{tot}(\rho, 0)|^2 = |E_{Incid}(\rho, 0)|^2 + |E_{Etalon}(\rho, 2d_{InP})|^2 + |E_{Incid}(\rho, 0)E_{Etalon}(\rho, 2d_{InP})| \cos \phi(\rho, 2d_{InP})$$

with

$$\phi(\rho, z) = k \frac{\rho^2}{2R(z)} + (kz - \zeta(z))$$

It is important to notice that few essential parameters of this model are simply unknown. For this reason the model needs to be “calibrated”. This is done by adjusting the electric field transmission  $\tau$  such that for a reference measurement the amplitude of the etaloning can be reproduced. After having adjusted  $\tau$  in the described way the following calculations can now be performed with modified values of the optical parameters of the incident beam (e.g., beam diameter, divergence angle, etc) while  $\tau$  is kept constant. The periodicity of the etaloning, however, is defined by the wavelength  $\lambda$  and the change of the optical path length of the etalon, i.e., the product of geometrical thickness and refractive index. A change could be raised by a slope of the etalon thickness, e.g., due to manufacturing tolerances.

For calibration of the model a beam diameter  $w_0$  of 13 $\mu\text{m}$  has been chosen, with its waist ideally placed at the front surface (SiNx) of the detector. The nominal thickness of the InP etalon is assumed, the value for refractive index  $n = 3.1453$  is taken from literature. The linear superposition of incident and reflected electric fields  $E_{tot}$  is calculated according to the formula above. The calculation is iterated while varying the etalon thickness in increments of 0.01 $\mu\text{m}$ . The results of the calculation for the reference measurement for both wavelengths  $\lambda_{on}$  and  $\lambda_{off}$  is shown in Figure 18. The amplitude of the etaloning of  $\sim 6\%$  is - within the measurement and model accuracy - in line with the measurement of Figure 13 c). In order to achieve this value a transmission factor  $\tau = 0.15$  of the electric field has been obtained, which correspond to a transmission of the power of  $I = |\tau E|^2 = 0.0225|E|^2$ .

For the full periodicity of the etaloning a thickness change of the InP etalon of  $\sim 260\text{nm}$  can be obtained from the reference plot, which is in line with the measured change of  $130\text{nm}$  (approx. half period; see previous section). This value may also be expressed in relative units, i.e., a change of  $260\text{nm}/188\mu\text{m} \sim 0.14\%$ . The root cause for etaloning can be either an optical thickness variation or simply a change of the wavelength by the same relative amount of - in this case -  $0.14\%$ . Taking  $\lambda_{on} = 1645,55\text{nm}$  as a reference wavelength, the spectral periodicity would be  $0.14\% \times \lambda_{on} \sim 2.3\text{nm}$ , which can be - at least approximately - seen in Figure 13 c).

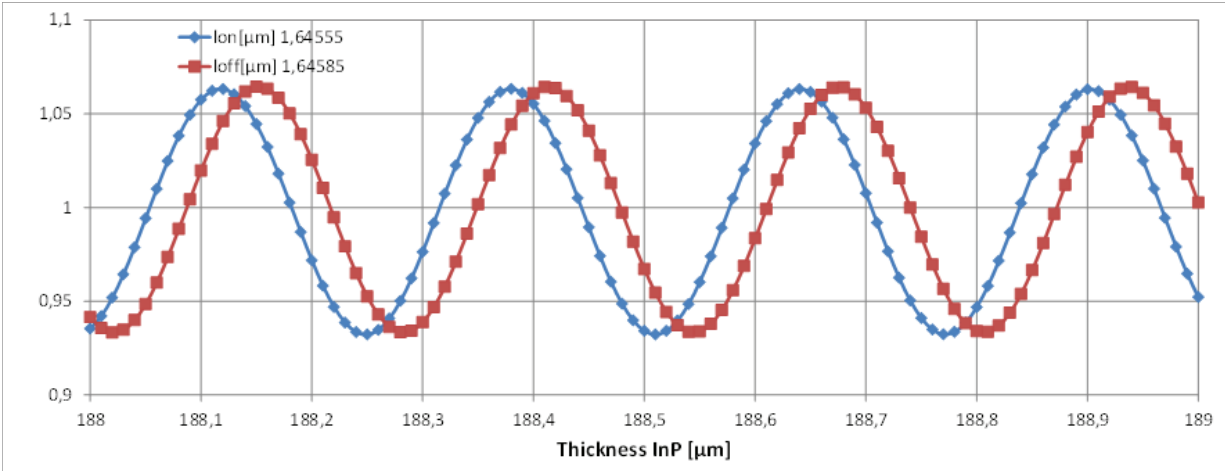


Figure 18 Results of the reference calculation for both wavelengths  $\lambda_{on}$  and  $\lambda_{off}$ .

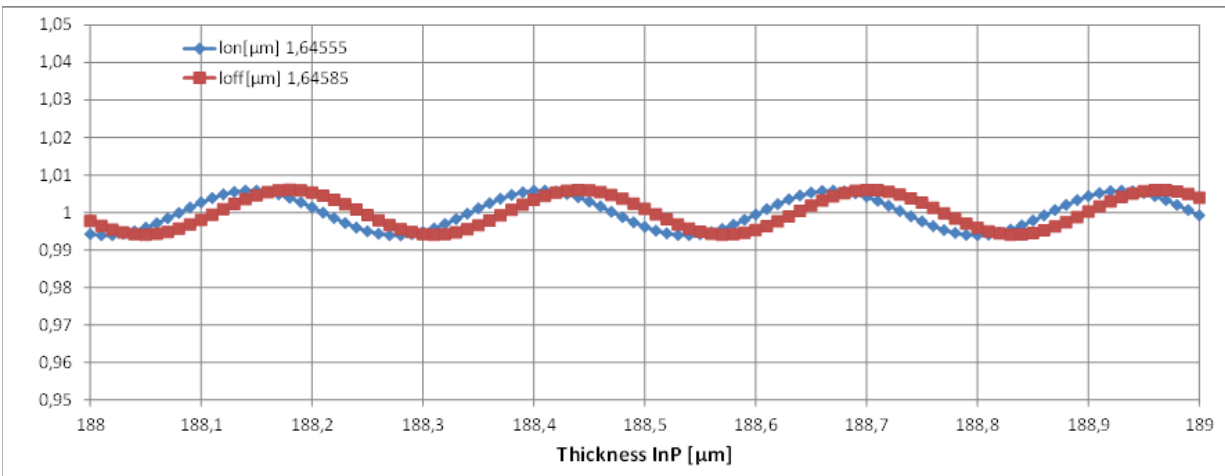


Figure 19 Results with a small beam diameter of  $3.4\mu\text{m}$ , which is much closer to the final flight configuration. The etaloning amplitude shrinks by nearly an order of magnitude.

The reduction of the beam diameter by a factor of  $\sim 4$  and an increase of the divergence angle by the same amount leads to a significant defocusing of the reflected electric field and thus to a much lower irradiance at the level of the InGaAs layer, where the two electric fields interfere. The important quantitative result is that shrinking the beam diameter by a significant factor and, consequently, increasing the cone (divergence) angle by the same amount reduces the variations of the radiometric measurements from  $\sim 12\%$  (P-V) to less than  $\sim 1.3\%$  (P-V).

### Impact on MERLIN SIC characterization and calibration test campaign

Based on the observed Etalon effect, the setup cannot be used as originally planned for the planned PFM radiometric resolution characterization and non-linearity calibration measurements. Based on the measurements and analysis the impact of the setup on the Etalon effect was understood and a way forward for the outstanding measurements was defined.

The PFM tests were originally planned with the 18.4mm focusing lens ( $\pm 8^\circ$  AOI). Based on the understanding of the Etalon effect, the 4.5mm lens will be used for radiometric calibration of the measurement system, together with the calibrated reference detector to correctly set the illumination level.

Afterwards the same 4.5mm lens will be used for radiometric resolution characterization and non-linearity calibration, since the illumination is determined based on this lens and it is considered representative enough in terms of AOI and resulting reduced etalon effect. The spot size will be approximately  $3.4\mu\text{m}$  (focused spot, default).

The non-linearity measurement will be repeated with an approximately  $60\mu\text{m}$  spot size (focus behind detector surface) as confirmation that no detrimental effects are observed by changed spot size.

## CONCLUSION

The joint (satellite and payload) MERLIN project performed in cooperation by CNES and DLR is currently in the middle of phase D, after successfully passing payload CDR in 2020. First (P)FM models of the different subsystems are already built and delivered to the instrument prime.

The second half of the paper summarizes investigations about an Etalon effect, which was identified in the frame of the QE scans for the PFM APD selection and which leads to an unexpected narrowband spectral, spatial and thermal dependence of the QE. The Etalon effect is caused by the InP substrate within the APD. The Etalon effect could be confirmed via test and simulation as root-cause for the unexpected QE behavior. This effect is strongly AOI dependent, which made a review of the scan setup necessary. The AOI was much smaller ( $\pm 8^\circ$ ) than the operational MERLIN PFM AOI ( $\pm 48^\circ$ ). Therefore, the setup was adapted via a stepwise increase of the AOI, which reduced and therefore confirmed the theory of the Etalon effect.

Spatial and spectral dependences of the APD QE are one contributor to the overall Relative Systematic Error. Therefore, it was important to check the new identified impact of this Etalon effect on the instrument performance.

Even for the largest achievable AOI in the setup to be used for calibration ( $4.5\text{mm} = \pm 30^\circ$ ) the Etalon effect is already smaller than the slope, which was assumed for the CDR. Therefore, the performance gets even better than expected until now and will even increase for the operational MERLIN AOI of  $\pm 48^\circ$ .

## ACKNOWLEDGEMENT

The authors would like to thank the whole MERLIN project team at DLR, CNES, Airbus DS, SpaceTech, Fraunhofer ILT, von Hoerner & Sulger, Safran Reosc and Laser Components Detector Group, Inc. for their continuous support and their fruitful cooperation in this challenging project. The German part of the MERLIN project is funded by the German Federal Ministry for Economic Affairs and Climate Action under DLR contract 50 EP 1601.

## REFERENCES

- [1] Ehret et al., „MERLIN: A French-German Space Lidar Mission Dedicated to Atmospheric Methane“ Remote Sens. 2017, 9, 1052
- [2] P. Flamant, G. Ehret, B. Millet, M. Alpers, “MERLIN: a French-German mission addressing methane monitoring by LIDAR from space”, Proc. of 26th ILRC, Porto Heli, Greece, (2012).

- [3] M. Bode, C. Wührer, M. Alpers, B. Millet, G. Ehret, P. Bousquet, "MERLIN: An Integrated Path Differential Absorption (IPDA) Lidar for Global Methane Remote Sensing", Proceedings of ICSO 2016, Biarritz, France 18-21 Oct. 2016.
- [4] Loehring, J. et al., Key optical components for spaceborne lasers, Proc. SPIE 9730, 2016
- [5] Hahn, S.; Bode, M.; Luttmann, J.; Hoffmann, H.-D., FULAS: high energy laser source for future lidar applications, Proc. SPIE 10562, 2017
- [6] S. Lucarelli, Andreas Allgaier, Martin Altenburg, Arnaud Chiri, Markus Bode, Alexander Fehringer, Victoria Hoefig, Christian Wuehrer, "Design, Development and Verification of the Merlin Payload", Proc. of the 14<sup>th</sup> European Conference on Space Structures, Material & Environmental Testing, Toulouse, September 27<sup>th</sup>-30<sup>th</sup>, 2016
- [7] S. Carli et al., "Structural Design Advantages of High Performance Radiators (HiPeR)", Proc. of the 15<sup>th</sup> European Conference on Space Structures, Material & Environmental Testing, ESA-ESTEC, Noordwijk, The Netherlands, 28 May – 1 June 2018
- [8] Sven Hahn, Markus Bode, Jörg Luttmann, Dieter Hoffmann, „FULAS: High energy laser source for future LIDAR applications” Proceedings of ICSO 2018, Crete, Greece Oct. 2018.
- [9] Susanne Nikolov, Werner Hupfer, Christian Wührer, Gerald Mathe, Alexander Sohmer, Stefano Lucarelli, Arnaud Chiri, Andreas Allgaier, Wolfgang Holota, Nicolas Paulin, “Robust optical design for optimal performance of the MERLIN Lidar instrument” Proceedings of ICSO 2018, Crete, Greece Oct. 2018.
- [10] S. Hahn, D. Kokkinos, C. Köhl, C. Wührer, J. Ammersbach, B. Gronloh, H. Hoffmann, P. Bartsch, „MERLIN High Energy Laser Source for Methane Sensing at 1645 nm”, Proceedings of ICSO 2022, Dubrovnik, Croatia, Oct. 2022.
- [11] C. Wührer, C. Köhl, S. Lucarelli, M. Bode, „MERLIN: overview of the design status of the Lidar Instrument“, Proceedings of ICSO2018, Crete, Greece Oct. 2018.